

ARTICLE

Investigation of the Lack of Angiogenesis in the Formation of Lymph Node Metastases

Han-Sin Jeong*, Dennis Jones*, Shan Liao, Daniel A. Wattson, Cheryl H. Cui, Dan G. Duda, Christopher G. Willett, Rakesh K. Jain, Timothy P. Padera

Affiliations of authors: Edwin L. Steele Laboratories, Department of Radiation Oncology, MGH Cancer Center, Massachusetts General Hospital and Harvard Medical School, Boston, MA (HSJ, DJ, SL, DAW, CC, DGD, RKJ, TPP); Department of Otorhinolaryngology-Head and Neck Surgery, Samsung Medical Center, Sungkyunkwan University School of Medicine, Seoul, South Korea (HSJ); Department of Radiation Oncology, Duke University Medical Center, Durham, NC (CGW).
Current affiliation: Department of Microbiology, Immunology and Infectious Diseases, University of Calgary, Calgary, Alberta, Canada (SL).

* Authors contributed equally to this work.

Correspondence to: Timothy P. Padera, PhD, Edwin L. Steele Laboratories, Department of Radiation Oncology, MGH Cancer Center, Massachusetts General Hospital and Harvard Medical School, 100 Blossom Street, Boston, Massachusetts 02114 (e-mail: tpadera@steele.mgh.harvard.edu).

Abstract

Background: To date, antiangiogenic therapy has failed to improve overall survival in cancer patients when used in the adjuvant setting (local-regional disease with no detectable systemic metastasis). The presence of lymph node metastases worsens prognosis, however their reliance on angiogenesis for growth has not been reported.

Methods: Here, we introduce a novel chronic lymph node window (CLNW) model to facilitate new discoveries in the growth and spread of lymph node metastases. We use the CLNW in multiple models of spontaneous lymphatic metastases in mice to study the vasculature of metastatic lymph nodes ($n = 9-12$). We further test our results in patient samples ($n = 20$ colon cancer patients; $n = 20$ head and neck cancer patients). Finally, we test the ability of antiangiogenic therapy to inhibit metastatic growth in the CLNW. All statistical tests were two-sided.

Results: Using the CLNW, we reveal the surprising lack of sprouting angiogenesis during metastatic growth, despite the presence of hypoxia in some lesions. Treatment with two different antiangiogenic therapies showed no effect on the growth or vascular density of lymph node metastases (day 10: untreated mean = 1.2%, 95% confidence interval [CI] = 0.7% to 1.7%; control mean = 0.7%, 95% CI = 0.1% to 1.3%; DC101 mean = 0.4%, 95% CI = 0.0% to 3.3%; sunitinib mean = 0.5%, 95% CI = 0.0% to 1.0%, analysis of variance $P = .34$). We confirmed these findings in clinical specimens, including the lack of reduction in blood vessel density in lymph node metastases in patients treated with bevacizumab (no bevacizumab group mean = 257 vessels/mm², 95% CI = 149 to 365 vessels/mm²; bevacizumab group mean = 327 vessels/mm², 95% CI = 140 to 514 vessels/mm², $P = .78$).

Conclusion: We provide preclinical and clinical evidence that sprouting angiogenesis does not occur during the growth of lymph node metastases, and thus reveals a new mechanism of treatment resistance to antiangiogenic therapy in adjuvant settings. The targets of clinically approved angiogenesis inhibitors are not active during early cancer progression in the lymph node, suggesting that inhibitors of sprouting angiogenesis as a class will not be effective in treating lymph node metastases.

Although antiangiogenic therapy is standard of care for several advanced (metastatic) cancers, all phase III clinical trials of antiangiogenic therapy to date have failed in the adjuvant setting (1-4). The presence of lymph node metastases—the

most common form of cancer dissemination—dictates treatment decisions (5,6), however their reliance on angiogenesis for growth has not been reported. Furthermore, observations from preclinical and clinical studies suggest that lymph node

metastases and primary tumors can respond differently to the same therapeutic regimen (7–9). The clinical relevance of lymph node metastases has been the subject of debate for many years. Some argue that the presence of lymph node metastasis only demonstrates the ability of the cancer to metastasize and that disease in the lymph node is inconsequential (10,11). The strong predictive power of lymph node metastases has led others to hypothesize that cancer cells in the lymph node can exit and spread to distant metastatic sites (12,13). These advocates argue disease in lymph nodes needs to be treated in order to prevent distant metastasis and ultimately eradicate disease from the patient (14,15). Likely the answer lies in between, depending where on the spectrum of progression to distant metastasis the cancer is diagnosed (16). These issues highlight our fundamental lack of understanding of the biology of how metastatic cancer cells grow in a lymph node and affect the overall prognosis for the patient, limiting our ability to discover effective adjuvant therapy to treat lymph node metastases.

We and others have previously shown that antiangiogenic therapy did not stop the seeding or growth of lymph node metastases (9,17,18), but no mechanism of failure has been determined. Nonsprouting angiogenesis mechanisms to sustain tumor growth, such as vessel co-option and intussusception, have been implicated in the growth of lung, liver, and brain metastases (19) and are thought to play a role in resistance to antiangiogenic therapy (20). Based on these findings, we hypothesized that early growth of lymph node metastases is not dependent on sprouting angiogenesis.

Although reports show reduced vascular density in lymph node metastases compared with corresponding primary tumors and surrounding normal lymph node (17,21,22), these data do not describe the degree of angiogenesis or whether the vessels are functional. Here, we introduce a novel model to longitudinally image the formation and growth of metastatic tumors in lymph nodes and reveal the surprising lack of sprouting angiogenesis, despite the presence of hypoxia in some lesions. Treatment with two different therapies designed to target sprouting angiogenesis showed no effect on the growth or vascular density of lymph node metastases in our models. These data are corroborated in clinical specimens and further add to mechanisms for the failure of antiangiogenic treatments in adjuvant settings (1–4,20).

Methods

Cell Lines and Animals

We used five different syngeneic tumor lines to study spontaneous metastatic lesions in lymph nodes covering three major diseases across four different immunocompetent mouse strains as described in the [Supplementary Methods](#) (available online). The animal experiment protocol was reviewed and approved by Institutional Animal Care and Use Committee of the Massachusetts General Hospital.

Lymph Node Window Model

To image the inguinal lymph node using intravital microscopy, we modified the chronic mammary fat pad window model (23,24) to create the chronic lymph node window (CLNW) (Figure 1; [Supplementary Figure 1](#), available online). The procedure is described in the [Supplementary Methods](#) (available online) is well tolerated with no detection of a change in animal body weight for up to 14 days after CLNW implantation.

Intravital Multiphoton Microscopy

Intravital multiphoton microscopy was carried out as described previously on a custom-built multiphoton microscope (25). Details of the imaging equipment, imaging protocols, and image analysis can be found in the [Supplementary Methods](#) (available online).

Immunohistochemical Staining

Clinical samples were obtained from archival specimens at the Massachusetts General Hospital (MGH) Department of Pathology, Duke University, and Samsung Medical Center. The study was approved by the MGH Institutional Review Board. Details of the staining protocols can be found in the [Supplementary Methods](#) (available online). We implemented a previously established image-processing algorithm to analyze vessel density and vessel area from CD31-immunostained histological lymph node sections (26–29) (CAIMAN, Sheffield University, UK, <http://caiman.group.shef.ac.uk/caiman/segment.php>). Tumor area and nontumor area were classified manually based on hematoxylin and eosin staining and Ki67 staining.

Evaluation of Anti-angiogenic Treatment

The initial volume of the metastatic lesions at random assignment to treatment and control groups was within a range of $5\text{--}10 \times 10^{-3} \text{ mm}^3$. The treatment regimens were: DC101 40mg/kg i.p. every third day (n = 5), sunitinib: 40mg/kg in 200 μL volume, oral gavage, every day (n = 6), IgG treatment (control for DC101) (n = 2), vehicle solution alone (control for sunitinib treatment) (n = 4), or no treatment (n = 12). We used the untreated mice as well as combined data from both control groups to form bases for comparison. Intravital multiphoton microscopy was performed in two- or three-day intervals, and the parameters for tumor and intratumoral vessels were generated by our automated custom MATLAB code to prevent bias.

Statistical Methods

Statistical significance was determined with either a one-way analysis of variance (ANOVA) with the Tukey's Honestly Significant Difference or Dunnett's post hoc test, two-tailed paired Student's *t* test, two-tailed unpaired Student's *t* test, or Mann-Whitney *U* test as appropriate. Statistical significance was set at $P < .05$. All statistical tests were two-sided. Data are presented as means with 95% confidence intervals (CI).

Results

Longitudinal Imaging of the Formation of Spontaneous Lymph Node Metastases Using a Novel Chronic Lymph Node Window

Holding back our understanding of the biology of lymph node metastasis is our inability to longitudinally monitor spontaneous lymph node metastases. Inspired by pioneering intravital microscopy of the lymph node (30–35), we developed a chronic lymph node window (CLNW)—a modification of the mammary fat pad chamber (23,24)—to create a CLNW that allows intravital imaging for up to 14 days with minimal morphological, cellular or biochemical changes in the inguinal lymph node (Figure 1, A and B; [Supplementary Figure 1](#), available online).

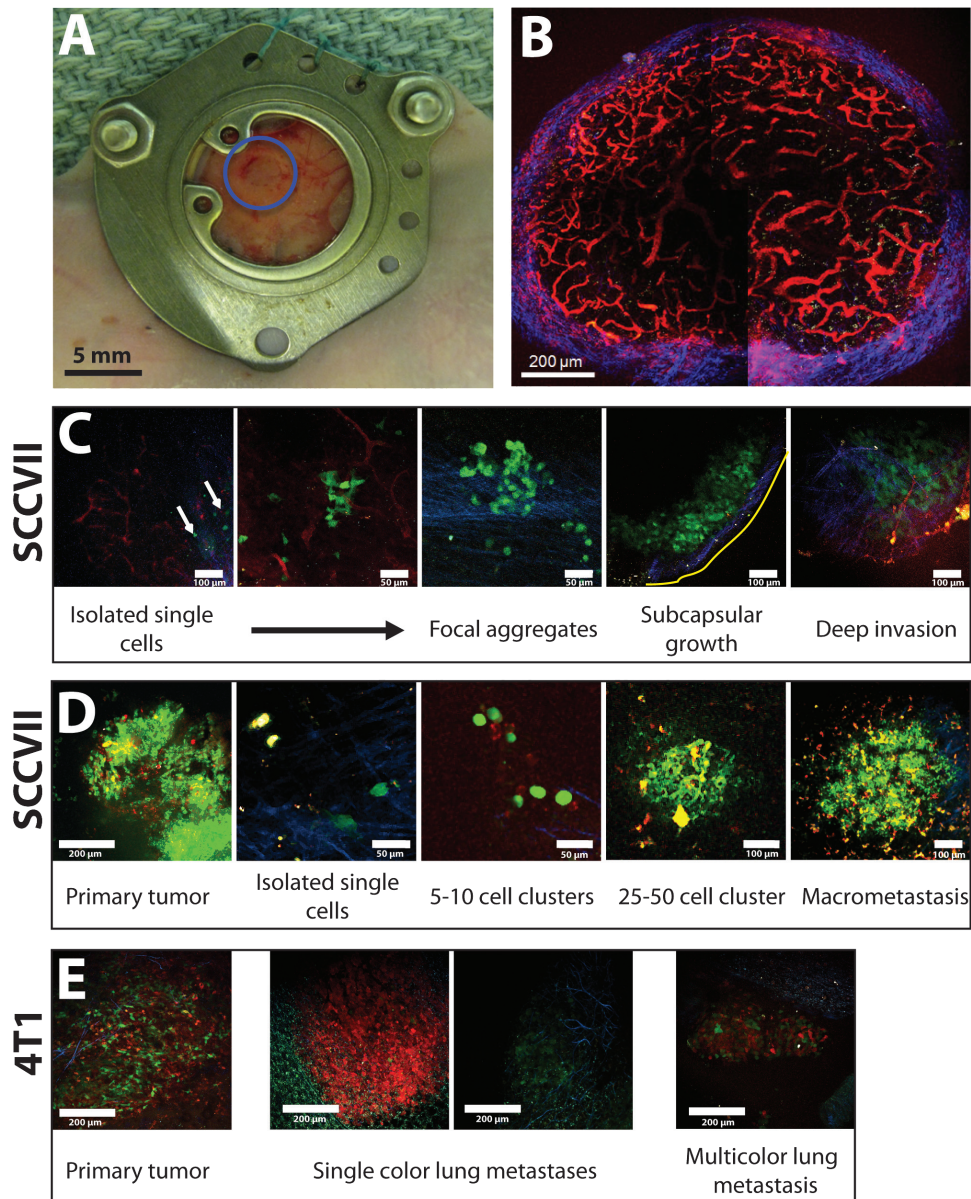


Figure 1. Growth of metastatic cancer cells in a lymph node. **A)** The chronic lymph node window (CLNW) allows stable intravital microscopy of the inguinal lymph node for up to 14 days. This procedure was well tolerated with no detection of a change in animal body weight for 14 days after CLNW implantation. **B)** TRITC-dextran angiography, imaged with multiphoton microscopy highlights the robust vasculature (red) of the inguinal lymph node. Second harmonic generation was used to highlight fibrillar collagen (blue) in the lymph node capsule. The image is a maximum intensity projection of 25 μm of tissue from inside the lymph node. **C)** Representative progression of the formation of lymph node metastasis (SCCVII) from the new arrival of isolated cancer cells (green) to the formation of small clusters of cells and finally their growth into tumors, initially near the capsule (blue) and then deeper in the lymph node near the pre-existing vasculature (red). The series of images was taken from multiple lymph nodes. Yellow line marks edge of lymph node. **D)** Using primary tumors (SCCVII) of multiple colors (red, green, yellow), we imaged the emergent multicolored lymph node metastasis ($n = 4$). **E)** Using primary tumors (4T1) of two colors (red, green) ($n = 4$), we found more than 80% of lung metastases contained just one color, with the rest consisting of two colors. Scale bars as indicated in each panel.

Using multiphoton microscopy in the CLNW, we were able to serially image various stages of the growth of spontaneous metastasis in the lymph node from murine SCCVII squamous cell carcinoma (36,37) transduced with green fluorescence protein (SCCVII-GFP) (Figure 1C). Initially, cancer cells remain in or near the subcapsular sinus as individual cells (Figure 1C). Later, small aggregates of a few cancer cells form near the subcapsular sinus, which then grow into metastatic lesions that invade deeper into the lymph node (Figure 1C). This sequence was also observed in syngeneic MCa-P0008 breast cancer and B16F10 melanoma cells lines (Supplementary Figure 2, available online).

Recent genomic studies suggest that metastatic cells within lymph nodes consist of multiple clones (38,39). To investigate this concept, we transduced SCCVII and SCCVII-GFP cells with a red fluorescence protein (DsRed), producing three different colors of cells (red, green, and red+green) that were mixed in equal proportions to form primary tumors. Single cells of multiple colors disseminated from the multicolor primary tumor and grew in the subcapsular sinus (Figure 1D). The metastatic lesions that subsequently formed contained all three colors with great spatial heterogeneity (Figure 1D), suggesting that lymph node metastases form from multiple cells. These findings were

reproduced when using an equal mix of 4T1-DsRed and 4T1-GFP mammary carcinoma cells implanted in the mammary fat pad. In contrast, more than 80% of detected lung metastases from these 4T1 tumors were single color (Figure 1E).

The Role of the Existing Lymph Node Vascular Supply in Supporting the Growth of Lymph Node Metastases

Next, we directly measured for the first time whether angiogenesis is occurring in lymph node metastases by using intravital multiphoton microscopy to make longitudinal measurements in our CLNW. In early stages, metastatic cells resided in the lymph node sinus, away from blood vessels (Figure 2A). These metastatic tumor cells eventually invaded the lymph node cortex, growing closer to functional lymph node blood vessels and presumably utilizing the nutrient supply of these pre-existing vessels (Figure 2A). We found that the tumor cells started to access host lymph node blood vessels when they invaded approximately 50 to 100 μm into the cortex (Figure 2, B and C). Although the tumor invaded deeper into the node (day 6 mean depth = 43 μm , 95% CI = 24 to 61 μm ; day 12 mean depth = 131 μm , 95% CI = 71 to 191 μm , $P = .01$), blood vessels did not invade toward the surface

of the lymph node (day 6 mean depth = 52 μm , 95% CI = 49 to 55 μm ; day 20 mean depth = 58 μm , 95% CI = 41 to 75 μm , $P = .38$), as would be expected for tumor-induced sprouting angiogenesis. These data provide the first direct evidence of the lack of sprouting angiogenesis during the growth of metastatic lesions in the lymph node.

Immunofluorescent staining for CD31 (Figure 3A) showed that the vessel density in lymph nodes with micrometastases from SCCVII tumors (Figure 3B) and macrometastases (lesions greater than 500 microns in one dimension) from 4T1 tumors (Figures 3E; Supplementary Figure 3A, available online) were not increased compared with those of control (from naïve mice with no tumor implantation) and contralateral nodes. The vessel density inside metastatic lesions was lower than the surrounding lymph node tissue (vessel density: SCCVII: metastatic lesion = 1.0%, 95% CI = 0.0% to 2.0%; nontumor area = 7.0%, 95% CI = 1.0% to 13.0%, $P = .04$; 4T1: metastatic lesion = 4.0%, 95% CI = 1.0% to 7.0%; nontumor area = 10.0%, 95% CI = 5.0% to 15.0%, $P = .04$) (Figure 3, C and F). To indicate sprouting angiogenesis, Ki67—a marker of cell proliferation—showed no difference in endothelial cell proliferation in micrometastatic lymph nodes (SCCVII) (Figure 3D; Supplementary Figure 4, available online) and a reduction in endothelial cell proliferation in macrometastatic lymph nodes (4T1) (Figure 3G; Supplementary Figure 3B,

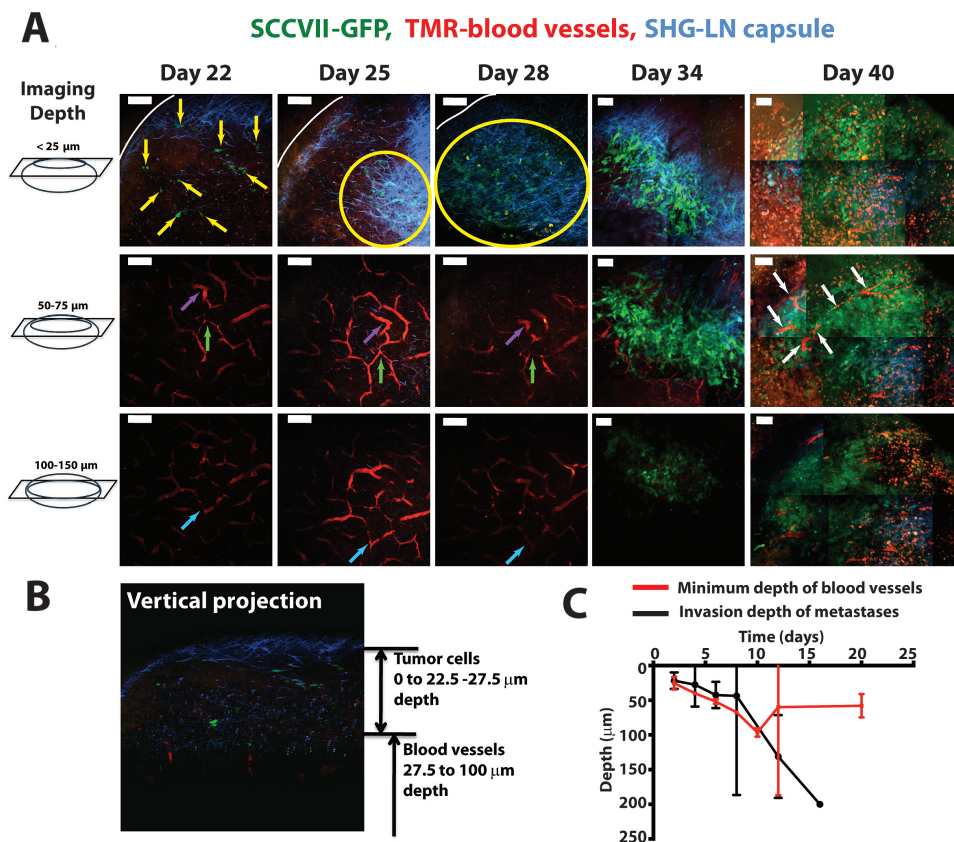


Figure 2. Intravital imaging of lymph node metastases and the native lymph node vasculature. A) Representative time course of images from a single metastatic lymph node, showing cancer cells (SCCVII, green) and blood vessels (TRITC-dextran, red) at three different depths in tissue. The image was created using multiphoton microscopy, and second harmonic generation was used to highlight fibrillar collagen (blue) in the lymph node capsule. The images are created from maximum intensity projections of 25 μm of tissue from inside the lymph node. In day 40 images, the red signal is background signal from the accumulation of TRITC-dextran as a result of the five intravenous injections over the course of the metastatic growth. Yellow arrows identify individual cancer cells. Yellow circles identify areas in which many cancer cells are found in the subcapsular sinus. White arrows identify blood vessels in the metastatic lesion. Purple, green and light blue arrows identify features in the lymph node vasculature that can be used to identify the same region in the mouse over the multiday experiment. White line marks edge of lymph node. Scale bars = 100 μm . B) A vertical image reconstruction showing the tumor cells (SCCVII, green) initially growing above the blood vessels (red). C) Measurements of the maximum depth of tumor cell invasion (SCCVII) and the minimum depth of blood vessels. Data are presented as mean \pm 95% confidence interval.

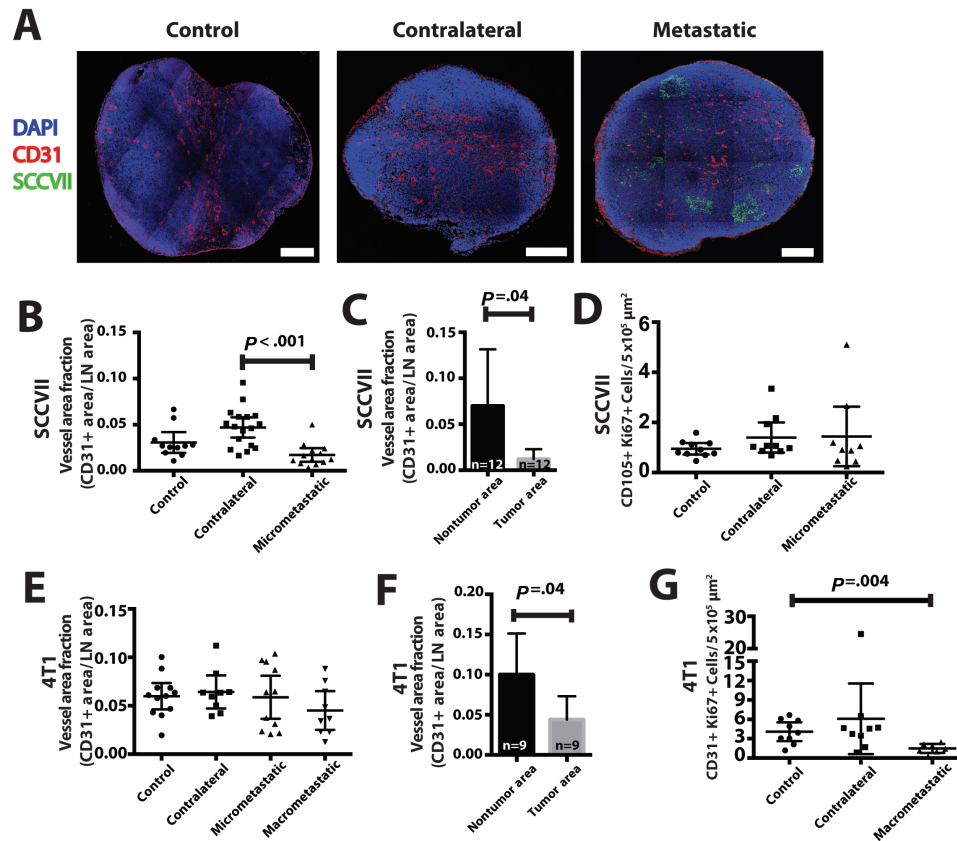


Figure 3. Immunohistochemical analysis of lymph node blood vessels and metastases. **A)** Representative sections of control (from non-tumor bearing mice), contralateral, and tumor-draining lymph nodes with micrometastases (SCCVII, green). Vessels were stained with CD31 (red) and nuclei with DAPI (blue). Scale bars = 300 μm . **B)** Quantification of CD31+ area per lymph node area in control, contralateral, and micrometastatic lymph nodes. **C)** In micrometastatic lymph nodes, quantification of CD31+ area per tissue area comparing tumor areas with nontumor areas. **D)** Costaining for CD105 and Ki67 measured blood vessel proliferation in micrometastatic lymph nodes. **E)** Using a different tumor model (4T1) that formed macrometastasis in the lymph node (greater than 500 μm in one direction), we measured CD31+ area in micrometastatic or macrometastatic lymph nodes, compared with control or contralateral nodes. **F)** The vascular area of macrometastatic lesions was measured in tumor areas and nontumor lymph node tissue. **G)** Costaining for CD31 and Ki67 measured blood vessel proliferation in macrometastatic lymph nodes. Data are presented as mean \pm 95% confidence interval. Statistical significance was tested by one-way analysis of variance with Tukey's Honestly Significant Difference post hoc test (B, D, E, G) or two-tailed paired Student's t test (C, F).

available online) in comparison with control and contralateral nodes. Vessel density in the metastatic lesions was not related to lesion size (Supplementary Figure 3C, available online). These data further indicate that sprouting angiogenesis is not induced in the lymph node at this stage of cancer progression.

In contrast, LYVE-1 staining for lymphatic vessels showed an increase in lymphatic vascular area (vessel density: SCCVII: control = 5.0%, 95% CI = 3.0% to 7.0%; contralateral = 8.0%, 95% CI = 6.0% to 10.0%; metastatic = 10.0%, 95% CI = 6.0% to 14.0%; control vs metastatic $P = .03$; 4T1: control = 5.0%, 95% CI = 2.0% to 8.0%; contralateral = 9.0%, 95% CI = 6.0% to 12.0%; nonmetastatic tumor draining = 22.0%, 95% CI = 18.0% to 26.0%; metastatic = 4.0%, 95% CI = 1.0% to 7.0%; control vs nonmetastatic tumor draining $P < .001$) and proliferating lymphatic endothelial cells in draining lymph nodes from SCCVII and 4T1 tumors (Supplementary Figures 5 and 6, available online), consistent with previous reports (40–43). Interestingly, the lymphatic vascular area was greater in the contralateral and nonmetastatic tumor-draining lymph nodes of 4T1-bearing mice compared with lymph nodes with macrometastatic lesions ($P < .001$) (Supplementary Figure 6, available online), suggesting that the presence of cancer cells causes the lymphatic vasculature to regress. When compared with lymph nodes from tumor-naïve animals, contralateral lymph nodes show greater lymphatic

vascular density (SCCVII: $P = .04$; 4T1: $P < .001$), suggesting that contralateral lymph nodes are also affected by the presence of the primary tumor, as others have reported (44).

Although lesions growing in the subcapsular sinus of the lymph node showed markers for hypoxia (Figure 4, A–D), sprouting angiogenesis was not induced in these lesions and they remained avascular. Metastatic lesions that invaded the lymph node parenchyma where functional nodal blood vessels reside had only focally heterogeneous areas positive for hypoxia markers (Figure 4, A, C, and E). These data suggest that growing metastatic lesions can utilize the existing lymph node vasculature in order to meet their metabolic demand. Whether this demand or hypoxia drives cancer cell invasion of the lymph node remains unknown.

Hypoxia generally induces the production of vascular endothelial growth factor (VEGF). However, VEGF levels in control, contralateral, and metastatic lymph nodes were not different (4T1: control = 0.3 pg VEGF/mg protein, 95% CI = 0.2 to 0.4 pg VEGF/mg protein; contralateral = 0.4 pg VEGF/mg protein, 95% CI = 0.3 to 0.5 pg VEGF/mg protein; metastatic = 0.5 pg VEGF/mg protein, 95% CI = 0.2 to 0.8 pg VEGF/mg protein; Figure 5A; SCCVII: control = 0.4 pg VEGF/mg protein, 95% CI = 0.3 to 0.5 pg VEGF/mg protein; contralateral = 0.4 pg VEGF/mg protein, 95% CI = 0.3 to 0.5 pg VEGF/mg protein; metastatic = 0.4 pg VEGF/mg protein, 95% CI = 0.3 to 0.5 pg VEGF/mg protein; Figure 5B; and

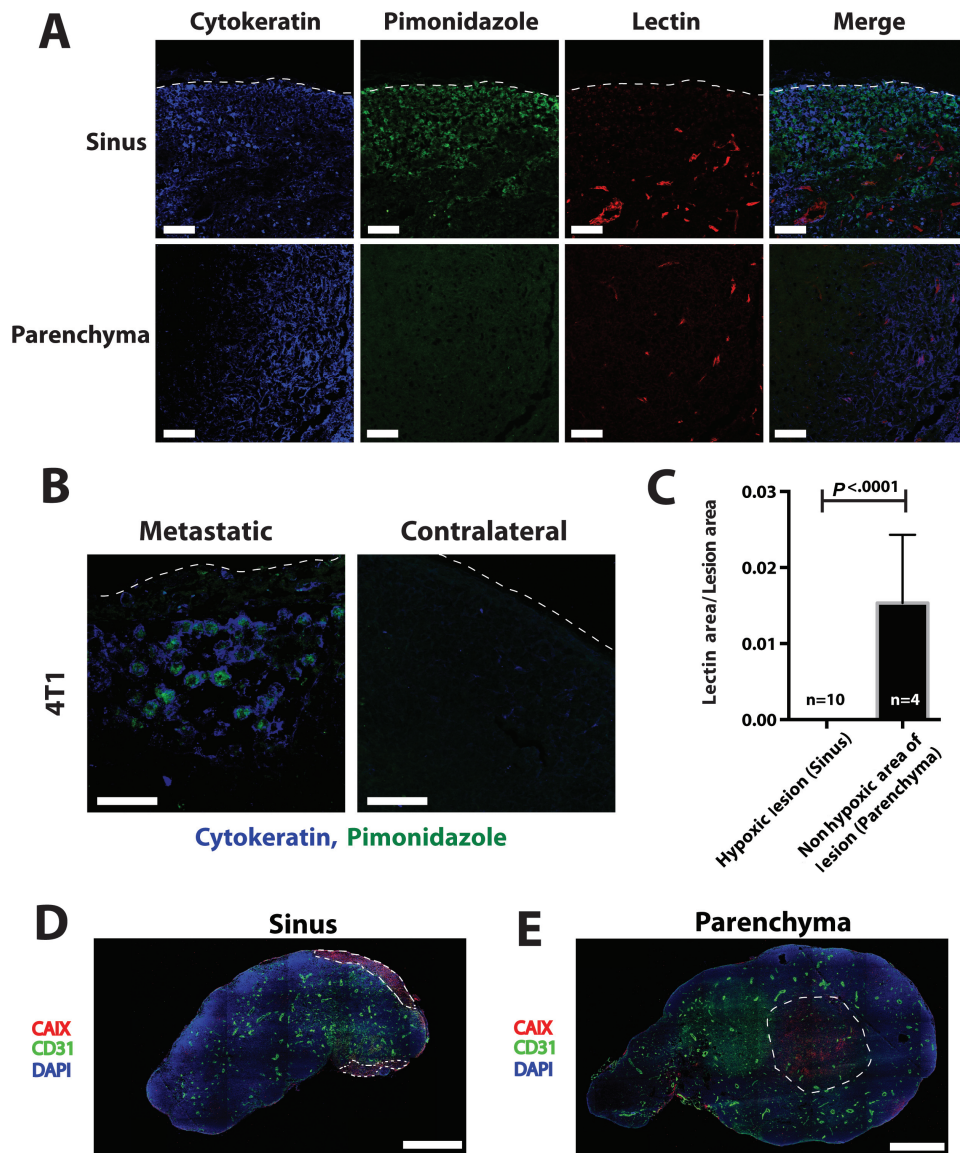


Figure 4. Hypoxia in lymph node metastases. **A)** Representative images of pimonidazole staining for hypoxia (green) and perfused lectin staining for functional blood vessels (red) in lymph node metastases from 4T1 mammary carcinoma (cytokeratin, blue). The top panels show a lesion in the subcapsular sinus that is hypoxic and has no perfused blood vessels in the lesion. The bottom panels show a lesion in the parenchyma of the lymph node with perfused blood vessels and no hypoxia. Dashed line shows edge of the lymph node. Scale bars = 100 μ m. **B)** Higher magnification of pimonidazole staining in metastatic lymph node showing colocalization of cytokeratin and pimonidazole. Contralateral lymph node is non-tumor bearing. Dashed line shows edge of the lymph node. Scale bars = 50 μ m. **C)** Quantification of pimonidazole and perfused vessel staining in metastatic lesions in the subcapsular sinus and lymph node parenchyma. Data are presented as mean \pm 95% confidence interval. Statistical significance was tested by two-tailed unpaired Student's *t* test. **D and E)** Staining for CAIX, a marker of the cellular response to hypoxia, and CD31-positive blood vessels shows similar results to pimonidazole staining. Dashed line shows the outline of the metastatic lesions. Scale bars = 636 μ m.

E0771: control = 0.3 pg VEGF/mg protein, 95% CI = 0.2 to 0.4 pg VEGF/mg protein; contralateral = 0.4 pg VEGF/mg protein, 95% CI = 0.3 to 0.5 pg VEGF/mg protein; metastatic = 0.4 pg VEGF/mg protein, 95% CI = 0.3 to 0.5 pg VEGF/mg protein; **Figure 5C**; all *P* values > .05 for each ANOVA containing these three lymph nodes types). Furthermore, levels of VEGF-C and VEGF-D were lower in metastatic and nonmetastatic tumor draining lymph nodes when compared with naïve lymph nodes (**Supplementary Figure 6, C and D**, available online). Next, we screened for transcriptional changes in sprouting angiogenesis-related genes in lymph nodes with metastasis when compared with naïve lymph nodes. No pro-angiogenesis related genes were upregulated in metastatic lymph nodes, but thrombospondin-1 (*Thbs-1*) and *TIMP-1*—both of which are antiangiogenic—were

upregulated (**Figure 5D**). We confirmed no change in *Vegf* levels (control = 0.24 VEGF/GAPDH, 95% CI = 0.06 to 0.42 VEGF/GAPDH; metastatic = 0.16 VEGF/GAPDH, 95% CI = 0.04 to 0.28 VEGF/GAPDH, *P* = .37) and the elevation in *Thbs-1* in lymph node metastasis by quantitative polymerase chain reaction (qPCR) (control = 0.10 *THBS-1*/GAPDH, 95% CI = 0.05 to 0.15 *THBS-1*/GAPDH; metastatic = 0.38 *THBS-1*/GAPDH, 95% CI = 0.23 to 0.53 *THBS-1*/GAPDH; *P* = .001) (**Figure 5E**). Thrombospondin-1 (*TSP-1*) was specifically located surrounding the blood vessels of control, contralateral, and metastatic lymph nodes (**Figure 5F**), further defining the nonangiogenic phenotype associated with these vessels. Taken together, these data describe an environment lacking pro-sprouting angiogenesis stimuli and abundant in antiangiogenesis molecules, suggesting metastatic lesions in

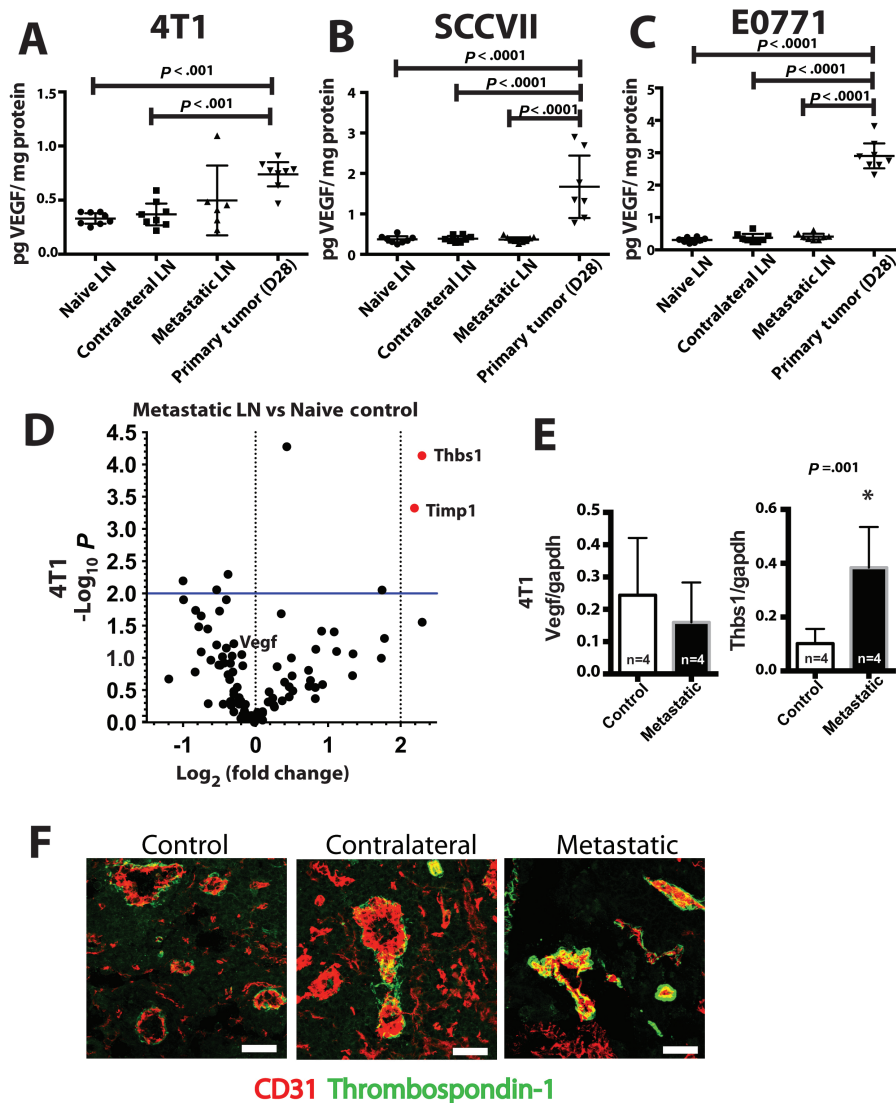


Figure 5. Molecular signature of quiescent lymph node vasculature. A-C) Levels of vascular endothelial growth factor (VEGF) protein were measured in metastatic lymph nodes containing 4T1 (A), SCCVII (B), or E0771 (C) and compared with control and contralateral lymph nodes. D) Quantitative polymerase chain reaction (qPCR) transcriptional array for angiogenesis-related genes compared the transcriptional profile of a diaeresis lymph node to a tumor-bearing lymph node. Differentially transcribed genes were defined as having more than a four-fold change and a P value under .01 when comparing metastatic lymph nodes to diaeresis lymph nodes. E) Confirmation of the qPCR transcriptional array for the *Vegf* and *Thbs1* genes. * $P < .05$. F) Dual immunofluorescence staining for CD31 (red) and TSP-1 (green) showed distinctive TSP-1 staining surrounding the blood vessels in diaeresis, contralateral, and metastatic lymph nodes. Scale bars = 100 μ m. Data are presented as mean \pm 95% confidence interval. Statistical significance was tested by one-way analysis of variance with Tukey's Honestly Significant Difference post hoc test (A, B, and C) and two-tailed unpaired Student's t test (E).

the lymph node do not induce nor rely upon sprouting angiogenesis during their early growth.

Blood Vessel Density in Metastatic Lymph Nodes From Colon Cancer and Head and Neck Cancer Patients

To confirm these findings in clinical specimens in a cancer where angiogenesis inhibitors have shown efficacy, we stained lymph nodes from 20 colon cancer patients with lymphatic metastasis for CD31 (Figure 6A; Supplementary Figure 7A, available online). These patients did not have metastases on initial staging and went directly for surgical resection with no prior cancer-directed treatments (eg, chemotherapy, radiation therapy). We found that

blood vessel densities in metastatic lymph nodes and large metastatic lesions where lymph node tissue was completely replaced with tumor cells were on average lower than those of tumor-negative lymph nodes (nonmetastatic = 220 blood vessels/mm², 95% CI = 172 to 268 blood vessels/mm²; metastatic = 135 blood vessels/mm², 95% CI = 113 to 157 blood vessels/mm²; lymph node replaced by cancer = 104 blood vessels/mm², 95% CI = 75 to 133 blood vessels/mm²; comparisons of either group of tumor-bearing to nonmetastatic lymph nodes: $P < .001$) (Figure 6, B and C). Furthermore, the vessel density inside metastatic lesions was statistically significantly lower than in the remaining lymph node tissue (metastatic lesion = 148 blood vessels/mm², 95% CI = 124 to 172 blood vessels/mm²; nontumor area = 115 blood vessels/mm², 95% CI = 95 to 135 blood vessels/mm², $P = .03$) (Figure 6, D and E). Accordingly, TSP-1 staining was also found

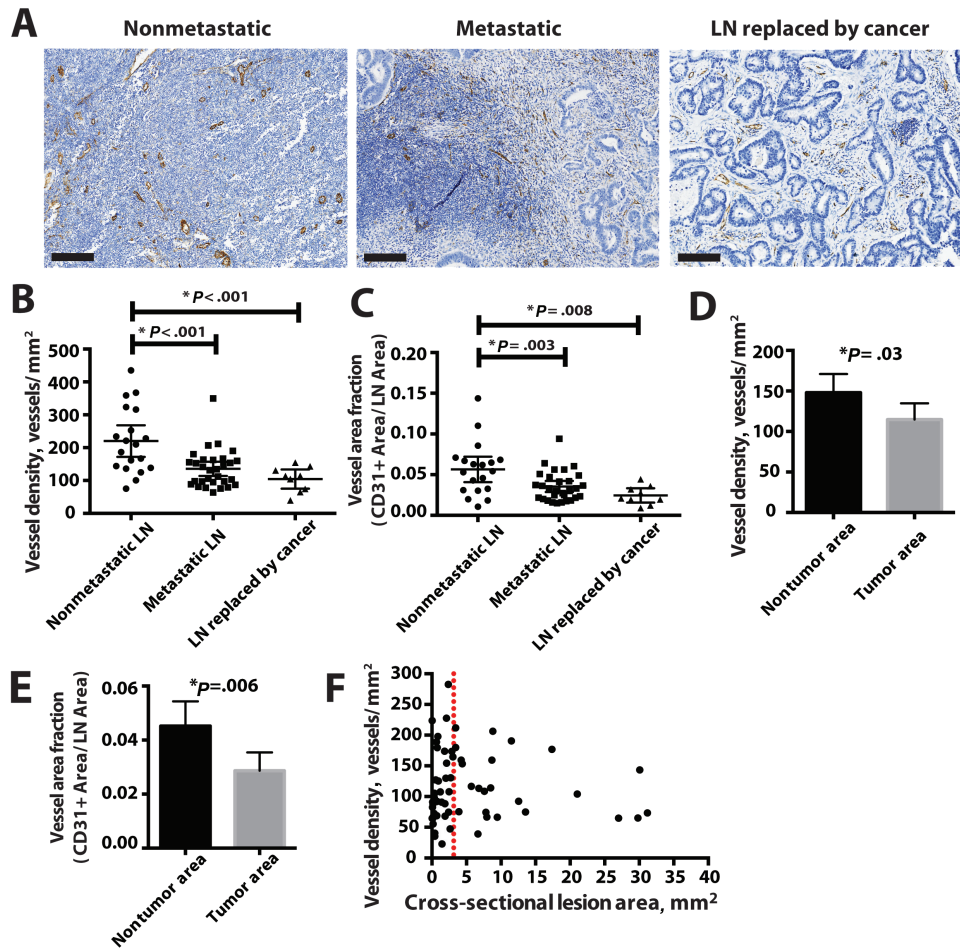


Figure 6. Vascular density in metastatic lymph nodes from colon cancer patients. **A)** Representative images of nonmetastatic ($n = 19$) and metastatic ($n = 39$) lymph nodes as well as lymph node tumors in which no normal lymph node tissue remained ($n = 9$). The sections were stained with CD31 (brown) to identify blood vessels. Scale bars = 200 μm . Images of whole lymph node sections can be found in [Supplementary Figure 7](#) (available online). **B)** The number of vessels per area as determined by CD31 staining was measured in metastatic lymph nodes and in lymph node tumors in which no normal lymph node tissue remained and compared with nonmetastatic lymph nodes. **C)** The fraction of lymph node area composed of CD31-positive vessels was similarly measured in metastatic lymph nodes and in lymph node tumors in which no normal lymph node tissue remained and compared with nonmetastatic lymph nodes. **D)** and **E)** Within a metastatic lymph node, vascular density (**D**) and vessel area fraction (**E**) were measured in the tumor and the nontumor area. **F)** Vessel density was not dependent on the lesion size. Data are presented as mean \pm 95% confidence interval throughout figure.

to associate with lymph node blood vessels and to surround the gland-like structures formed by the cancer cells ([Supplementary Figure 7B](#), available online), further suggesting that these vessels were not undergoing sprouting angiogenesis. Finally, the density of CD31-positive vessels was not dependent on the lesion size in the section, showing that vessel densities of macrometastases (clinically classified as lesions larger than 2 mm in one direction [45]) are the same as in micrometastases ([Figure 6F](#)). Blood vessel density and TSP-1 staining in specimens from head and neck cancer patients were similar to those from colon cancer patients ([Supplementary Figure 7, C–G](#), available online). Taken together, these data from two different patient populations support the concept that the growth of metastatic lesions in the lymph nodes is not dependent upon sprouting angiogenesis.

Growth of Lymph Node Metastases With Antiangiogenic Treatment

To directly measure the response of lymph node metastases to antiangiogenic therapy in the CLNW, we began treatment when

micrometastases were between 100 and 125 μm in diameter ($5\text{--}10 \times 10^{-3} \text{ mm}^3$)—the stage when we found blood vessels surrounding lymph node metastases—with either a monoclonal VEGF receptor (VEGFR)-2-blocking antibody (DC101, ImClone Systems) or the pan-VEGFR small-molecule tyrosine kinase inhibitor sunitinib. We chose agents with differential mechanisms of VEGF pathway inhibition—monoclonal antibody vs tyrosine kinase inhibitor (TKI)—to understand whether our findings were agent specific. Measuring lymph node blood vessels using the CLNW and longitudinal multiphoton microscopy, the growth of lymph node metastases ([Figure 7, A–C](#)) and functional blood vessel volume density remained at similar levels during treatment with either DC101 or sunitinib when compared with untreated controls (vessel density: day 10: untreated = 1.2%, 95% CI = 0.7% to 1.7%; control = 0.7%, 95% CI = 0.1% to 1.3%; DC101 = 0.4%, 95% CI = 0.0% to 3.3%; sunitinib = 0.5%, 95% CI = 0.0% to 1.0%; ANOVA $P = .34$) ([Figure 7D](#)). These direct measurements, supported by previous endpoint studies (9,17), suggest that inhibitors of sprouting angiogenesis as a class of drugs will not be effective in inhibiting the early phase of lymph

node metastasis. In contrast, sunitinib—a pan-VEGF receptor TKI—reduced the elevated lymphatic vessel density found in early metastatic lymph nodes compared with PBS control (Supplementary Figure 8, available online).

Blood Vessel Density of Lymph Node Metastasis From Patients Treated With Bevacizumab

Finally, we identified rectal cancer patients that received neoadjuvant chemoradiation and bevacizumab and a comparator cohort of rectal cancer patients who received only neoadjuvant chemoradiation, as previously described (46,47). Despite downstaging of the primary tumor after neoadjuvant therapy, lymph node metastases were often found at the time of surgery and pathological evaluation. Comparing lymph node metastases from 10 patients in each group, we found no difference in the vessel density in lymph node metastases (no bevacizumab group mean = 257 vessels/mm², 95% CI = 149 to 365 vessels/mm²; bevacizumab group mean = 327 vessels/mm², 95% CI = 140 to 514 vessels/mm², *P* = .78) (Figure 8, A and B). The vascular density

in the tumor lesions specifically was also not different between the groups (no bevacizumab group mean = 307 blood vessels/mm², 95% CI = 186 to 428 vessels/mm²; bevacizumab group mean = 318 blood vessels/mm², 95% CI = 118 to 518 vessels/mm², *P* = .60) (Figure 8, C and D). Metastatic lymph nodes showed lower vascular density than nonmetastatic nodes after neoadjuvant therapy (Figure 8, A and B), independent of whether bevacizumab was used. Finally, lymphatic vessel density was not different in metastatic and nonmetastatic lymph nodes when comparing patients who received bevacizumab to those who did not (Supplementary Figure 8, D and E, available online). These data provide the first clinical evidence for the lack of response of lymph node metastasis to antiangiogenic therapy.

Discussion

The main concept driving antiangiogenic therapy has been the hypothesis that tumors depend on new blood vessel growth. A critical observation made by longitudinal intravital microscopy in the CLNW is that metastatic lesions did not induce

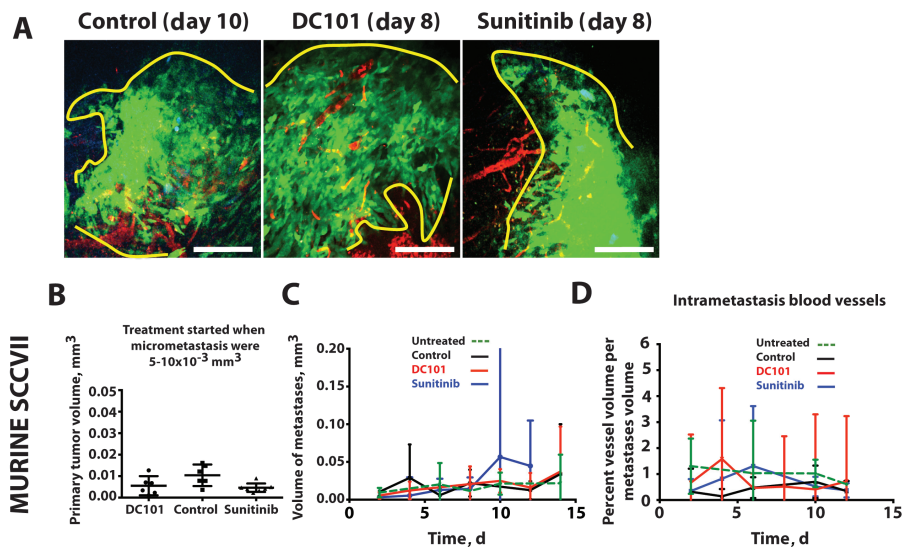


Figure 7. Antiangiogenic therapy in the early growth of lymph node metastases. **A)** Representative intravital multiphoton microscopy images of spontaneous lymph node metastases treated with vehicle control, sunitinib, or the blocking monoclonal anti-VEGF-2 antibody DC101. Tumor cells are shown in green and blood vessels in red. Scale bars = 200 μm . **B)** Primary tumors were of equal size at the time treatment began, when the lymph node micrometastases were $5\text{--}10 \times 10^{-3} \text{ mm}^3$. **C)** The growth rate of the metastatic tumor in the lymph node was measured during antiangiogenesis therapy. **D)** The vessel density in metastatic lesions in the lymph node was measured during antiangiogenesis therapy. Biological replicates: untreated *n* = 15 (C), 12 (D), control (IgG = 2, PBS = 4) *n* = 6, sunitinib = 6, DC101 = 5. Data are presented as mean \pm 95% confidence interval. Statistical significance was tested by one-way analysis of variance with Tukey's Honestly Significant Difference post hoc test (B and C) and two-tailed unpaired Student's *t* test (D and E).

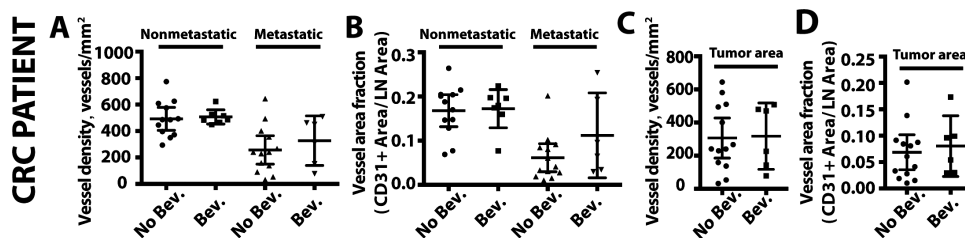


Figure 8. Vascular density in lymph node metastases in rectal cancer patients treated with bevacizumab. The number of CD31+ vessels per area (A) and the fraction of lymph node area composed of CD31+ vessels (B) were measured in nonmetastatic and metastatic lymph nodes in colorectal cancer (CRC) patients that received neoadjuvant chemoradiation (No Bev.) or neoadjuvant chemoradiation with bevacizumab (Bev.). *P* value was determined by two-tailed unpaired Student's *t* test. C and D) Within the tumor area of metastatic lymph nodes, we measured vascular density (C) and vessel area fraction (D) in rectal cancer patients that received neoadjuvant chemoradiation (No Bev.) or neoadjuvant chemoradiation with bevacizumab (Bev.). *P* value was determined by two-tailed unpaired Student's *t* test. Data are presented as mean \pm 95% confidence interval.

sprouting angiogenesis as they grew, in spite of the presence of hypoxia. Lesions that invaded into the blood vessel-rich lymph node parenchyma showed reduced hypoxia, suggesting that cancer cells survive in the lymph node by utilizing the existing lymph node vascular supply. The lack of VEGF, VEGF-C, and VEGF-D, along with the presence of TSP-1 surrounding lymph node blood vessels, provides a mechanism behind the lack of sprouting angiogenesis observed in lymph node metastases. A limitation of the use of longitudinal intravital microscopy is the limited imaging depth of 300 μm by multiphoton microscopy in the CLNW. To balance this, we used histological techniques, which allow full lymph node depth to be characterized but are limited in their ability to monitor the kinetic changes occurring as metastatic lesions grow in the lymph node. Using these complementary techniques allowed better characterization of the growth of lymphatic metastases.

Our data show lymph node lymphangiogenesis is an early event in the natural history of cancer progression, in agreement with previous studies (40,41,43). However, decreased lymphatic vessel density was found in macrometastatic lymph nodes, suggesting that the presence of the cancer cells in the lymph node causes lymphatic vessel regression. Furthermore, bevacizumab did not statistically significantly affect the lymphatic vasculature in patients. These data suggest that late intervention with antiangiogenic or antilymphangiogenic therapies after lymphatic vessel regression has begun in patients will show no effect on lymph node lymphatic vessels.

In patients, the observation that large metastatic lesions do not exhibit increased vascular density relative to those with micrometastases further suggests that sprouting angiogenesis is not required to sustain the growth of lymph node metastases. A limitation of our data is that we estimated lesion size based on the two-dimensional area available in the histological sections, so we are likely underestimating the size of the lesion. An additional limitation of our study is that we cannot rule out the contribution from different modes of new blood vessel formation in lymph node metastasis such as vasculogenesis, intussusception, vessel co-option, vascular mimicry, and tumor cell differentiation into endothelial cells (20). The mechanisms of these alternative processes are not clearly defined, although VEGF and endothelial proliferation have been shown to contribute to these processes (48–51). Our preclinical and clinical data, however, show that inhibitors targeting primarily sprouting angiogenesis will not inhibit the growth of metastases in the lymph node.

Predicted by recent genomic data (38,39,52), we provide direct evidence that lymph node metastasis forms from multiple cells that disseminate from the primary tumor and suggest a fundamental difference in their formation compared with hematogenous metastases. Cancer cells that invade lymphatic vessels travel to the draining lymph node where they enter in locations defined by afferent lymphatic vessels. As such, lymph node metastasis can be reinforced by the continual arrival of new cells as they gain a foothold in their new microenvironment, leading to the spatially heterogeneous lesions imaged here and the genetically heterogeneous lesions documented previously (38,39,52,53). In contrast, cells that metastasize through the blood spread out to different locations in an organ by the branching vasculature, leading to a higher probability of individually homogenous lesions. One can thus speculate that targeting a single genetic trait, unless ubiquitous in the primary tumor, may not be effective in eradicating lymph node metastases and any subsequent spread to distant sites (39).

Using multiple spontaneous metastasis models, we show the first direct evidence that sprouting angiogenesis is not required

in lymph node lesions during early metastatic growth. The lack of sprouting angiogenesis in lymph node metastases suggests an additional explanation for the poor outcomes of antiangiogenic therapy in adjuvant settings. As the lymph node is able to metabolically support rapid cellular expansion during an active immune response, it seems the existing vasculature of the lymph node is also able to support the growth of a nascent metastasis. Thus, the mechanisms of angiogenesis and the targets of clinically approved drugs are not active during this early step in cancer progression, suggesting that inhibitors of sprouting angiogenesis as a class will not be effective in treating lymph node metastases. Our novel preclinical models provide opportunities to uncover strategies to better control and eradicate disease in lymph nodes in metastatic cancer patients.

Funding

This work was supported by the National Institute of Health DP2OD008780 (TPP), R00CA137167 (TPP), National Cancer Institute (NCI) Federal Share/MGH Proton Beam Income on C06 CA059267 (TPP, RKJ), P01 CA080124 (RKJ), and R01-CA159258 (DGD). This work was also supported in part by the US Department of Defense CDMRP W81XWH-10-1-0016 (RKJ), the National Foundation for Cancer Research (RKJ), American Cancer Society grant 120733-RSG-11-073-01-TBG (DGD), Korean MEST NRF-2012R1A1A2040866 (HJ), Samsung Biomedical Research Institute Grant #GL1B22912 (HJ), United Negro College Fund–Merck Science Initiative Postdoctoral Fellowship (DJ), Burroughs Wellcome Postdoctoral Enrichment Program Award (DJ), National Institutes of Health (NIH) NCI F32CA183465 (DJ), Charles A. King Trust Fellowship (SL) and NIH K99HL111343-01A1 (SL).

Notes

The study funders had no role in the design of the study, the collection, analysis, or interpretation of the data, the writing of the manuscript, nor the decision to submit the manuscript for publication.

The authors would like to thank Dr. Gregory Lauwers for his assistance in obtaining clinical specimens. We would like to thank Dr. Constantino Carlos Reyes-Aldasoro of the School of Engineering and Mathematical Sciences at City University London for generously providing his novel code for identifying blood vessels in immunohistochemically stained tissue. We would like to thank ImClone Systems/Eli Lilly for reagents. We would like to thank Drs. Rosa Ng and Benjamin Vakoc for support and helpful comments on the manuscript.

HSJ, DJ, SL, DAW, CC, CGW, and TPP declare no conflicts of interest. RKJ is on the Board of Directors of Xtuit, serves as a consultant to Ophthotech, PureTech, Scholarly Publishing and Academic Resources Coalition, and SynDevRx, holds equity in Enlight, Ophthotech, SynDevRx, and Xtuit, has received research funding from Dyax, Medimmune, and Roche, and serves on the Board of Trustees of Tekla Healthcare Investors, Tekla Life Sciences Investors, and Tekla Healthcare Opportunities Fund. D.G.D. consults for Hexal/Sandoz and has received research funding from Merrimack. None of these interests pose a conflict for this work

References

- Allegra CJ, Yothers G, O'Connell MJ, et al. Phase III trial assessing bevacizumab in stages II and III carcinoma of the colon: results of NSABP protocol C-08. *J Clin Oncol*. 2011;29(1):11–16.

2. Cameron D, Brown J, Dent R, et al. Adjuvant bevacizumab-containing therapy in triple-negative breast cancer (BEATRICE): primary results of a randomised, phase 3 trial. *Lancet Oncol.* 2013;14(10):933–942.
3. de Gramont A, Van Cutsem E, Schmoll HJ, et al. Bevacizumab plus oxaliplatin-based chemotherapy as adjuvant treatment for colon cancer (AVANT): a phase 3 randomised controlled trial. *Lancet Oncol.* 2012;13(12):1225–1233.
4. Jain RK. Antiangiogenesis strategies revisited: from starving tumors to alleviating hypoxia. *Cancer Cell.* 2014;26(5):605–622.
5. Kawada K, Taketo MM. Significance and mechanism of lymph node metastasis in cancer progression. *Cancer Res.* 2011;71(4):1214–1218.
6. Edge SB, Byrd DR, Compton CC, et al. *AJCC Cancer Staging Manual*. In. 7th ed. New York: Springer; 2010.
7. Akita H, Doki Y, Yano M, et al. Effects of neoadjuvant chemotherapy on primary tumor and lymph node metastasis in esophageal squamous cell carcinoma: additive association with prognosis. *Dis Esophagus.* 2009;22(4):291–297.
8. Medich D, McGinty J, Parda D, et al. Preoperative chemoradiotherapy and radical surgery for locally advanced distal rectal adenocarcinoma: pathologic findings and clinical implications. *Dis Colon Rectum.* 2001;44(8):1123–1128.
9. Padera TP, Kuo AH, Hoshida T, et al. Differential response of primary tumor versus lymphatic metastasis to VEGFR-2 and VEGFR-3 kinase inhibitors cediranib and vandetanib. *Mol Cancer Ther.* 2008;7(8):2272–2279.
10. Cady B. Regional lymph node metastases: a singular manifestation of the process of clinical metastases in cancer: contemporary animal research and clinical reports suggest unifying concepts. *Ann Surg Oncol.* 2007;14(6):1790–1800.
11. Fisher B, Jeong JH, Anderson S, et al. Twenty-five-year follow-up of a randomized trial comparing radical mastectomy, total mastectomy, and total mastectomy followed by irradiation. *N Engl J Med.* 2002;347(8):567–575.
12. Halsted WS. I. The Results of Radical Operations for the Cure of Carcinoma of the Breast. *Ann Surg.* 1907;46(1):1–19.
13. Cascinelli N, Morabito A, Santinami M, et al. Immediate or delayed dissection of regional nodes in patients with melanoma of the trunk: a randomised trial. *WHO Melanoma Programme.* *Lancet.* 1998;351(9105):793–796.
14. Clarke M, Collins R, Darby S, et al. Effects of radiotherapy and of differences in the extent of surgery for early breast cancer on local recurrence and 15-year survival: an overview of the randomised trials. *Lancet.* 2005;366(9503):2087–2106.
15. Morton DL, Thompson JF, Cochran AJ, et al. Final trial report of sentinel-node biopsy versus nodal observation in melanoma. *N Engl J Med.* 2014;370(7):599–609.
16. Hellman S. Karmofsky Memorial Lecture. Natural history of small breast cancers. *J Clin Oncol.* 1994;12(10):2229–2234.
17. Roberts N, Kloos B, Cassella M, et al. Inhibition of VEGFR-3 activation with the antagonistic antibody more potently suppresses lymph node and distant metastases than inactivation of VEGFR-2. *Cancer Res.* 2006;66(5):2650–2657.
18. Matsumoto M, Roufail S, Inder R, et al. Signaling for lymphangiogenesis via VEGFR-3 is required for the early events of metastasis. *Clin Exp Metastasis.* 2013;30(6):819–832.
19. Donnem T, Hu J, Ferguson M, et al. Vessel co-option in primary human tumors and metastases: an obstacle to effective anti-angiogenic treatment? *Cancer Med.* 2013;2(4):427–436.
20. Carmeliet P, Jain RK. Molecular mechanisms and clinical applications of angiogenesis. *Nature.* 2011;473(7347):298–307.
21. Arapandoni-Dadioti P, Giatromanolaki A, Trihia H, et al. Angiogenesis in ductal breast carcinoma. Comparison of microvessel density between primary tumour and lymph node metastasis. *Cancer Lett.* 1999;137(2):145–150.
22. Naresk KN, Nerurkar AY, Borges AM. Angiogenesis is redundant for tumour growth in lymph node metastases. *Histopathology.* 2001;38(5):466–470.
23. Kedrin D, Gligorijevic B, Wyckoff J, et al. Intravital imaging of metastatic behavior through a mammary imaging window. *Nat Methods.* 2008;5(12):1019–1021.
24. Chauhan VP, Stylianopoulos T, Martin JD, et al. Normalization of tumour blood vessels improves the delivery of nanomedicines in a size-dependent manner. *Nat Nanotechnol.* 2012;7(6):383–388.
25. Brown EB, Campbell RB, Tsuzuki Y, et al. In vivo measurement of gene expression, angiogenesis and physiological function in tumors using multiphoton laser scanning microscopy. *Nat Med.* 2001;7(7):864–868.
26. Reyes-Aldasoro CC, Williams LJ, Akerman S, et al. An automatic algorithm for the segmentation and morphological analysis of microvessels in immunostained histological tumour sections. *J Microsc.* 2011;242(3):262–278.
27. Reyes-Aldasoro CC, Bjordahl MA, Akerman S, et al. Online chromatic and scale-space microvessel-tracing analysis for transmitted light optical images. *Microvasc Res.* 2012;84(3):330–339.
28. Reyes-Aldasoro CC, Griffiths MK, Savas D, et al. CAIMAN: an online algorithm repository for Cancer Image Analysis. *Comput Methods Programs Biomed.* 2011;103(2):97–103.
29. Reyes-Aldasoro CC. Retrospective shading correction algorithm based on signal envelope estimation. *Electron Lett.* 2009;45(9):454–456.
30. Mempel TR, Henrickson SE, Von Andrian UH. T-cell priming by dendritic cells in lymph nodes occurs in three distinct phases. *Nature.* 2004;427(6970):154–159.
31. Miller MJ, Wei SH, Parker I, et al. Two-photon imaging of lymphocyte motility and antigen response in intact lymph node. *Science.* 2002;296(5574):1869–1873.
32. Mora JR, Bono MR, Manjunath N, et al. Selective imprinting of gut-homing T cells by Peyer's patch dendritic cells. *Nature.* 2003;424(6944):88–93.
33. Stoll S, Delon J, Brotz TM, et al. Dynamic imaging of T cell-dendritic cell interactions in lymph nodes. *Science.* 2002;296(5574):1873–1876.
34. von Andrian UH. Intravital microscopy of the peripheral lymph node microcirculation in mice. *Microcirculation.* 1996;3(3):287–300.
35. Ito K, Smith BR, Parashurama N, et al. Unexpected dissemination patterns in lymphoma progression revealed by serial imaging within a murine lymph node. *Cancer Res.* 2012;72(23):6111–6118.
36. Hirst DG, Brown JM, Hazlehurst JL. Enhancement of CCNU cytotoxicity by misonidazole: possible therapeutic gain. *Br J Cancer.* 1982;46(1):109–116.
37. Kallman RF, Silini G, Van Putten LM. Factors influencing the quantitative estimation of the in vivo survival of cells from solid tumors. *J Natl Cancer Inst.* 1967;39(3):539–549.
38. Campbell PJ, Yachida S, Mudie LJ, et al. The patterns and dynamics of genomic instability in metastatic pancreatic cancer. *Nature.* 2010;467(7319):1109–1113.
39. McFadden DG, Papagiannakopoulos T, Taylor-Weiner A, et al. Genetic and clonal dissection of murine small cell lung carcinoma progression by genome sequencing. *Cell.* 2014;156(6):1298–1311.
40. Hirakawa S, Kodama S, Kunstfeld R, et al. VEGF-A induces tumor and sentinel lymph node lymphangiogenesis and promotes lymphatic metastasis. *J Exp Med.* 2005;201(7):1089–1099.
41. Hirakawa S, Brown LF, Kodama S, et al. VEGF-C-induced lymphangiogenesis in sentinel lymph nodes promotes tumor metastasis to distant sites. *Blood.* 2007;109(3):1010–1017.
42. Garmy-Susini B, Avraamides CJ, Desgrosellier JS, et al. PI3Kalpha activates integrin alpha4beta1 to establish a metastatic niche in lymph nodes. *Proc Natl Acad Sci U S A.* 2013;110(22):9042–9047.
43. Harrell MI, Iritani BM, Ruddell A. Tumor-induced sentinel lymph node lymphangiogenesis and increased lymph flow precede melanoma metastasis. *Am J Pathol.* 2007;170(2):774–786.
44. Ozasa R, Ohno J, Iwahashi T, et al. Tumor-induced lymphangiogenesis in cervical lymph nodes in oral melanoma-bearing mice. *J Exp Clin Cancer Res.* 2012;31:83.
45. Huvos AG, Hutter RV, Berg JW. Significance of axillary macrometastases and micrometastases in mammary cancer. *Ann Surg.* 1971;173(1):44–46.
46. Willett CG, Boucher Y, di Tomaso E, et al. Direct evidence that the VEGF-specific antibody bevacizumab has antivascular effects in human rectal cancer. *Nat Med.* 2004;10(2):145–147.
47. Willett CG, Duda DG, Ancukiewicz M, et al. A safety and survival analysis of neoadjuvant bevacizumab with standard chemoradiation in a phase I/II study compared with standard chemoradiation in locally advanced rectal cancer. *Oncologist.* 2010;15(8):845–851.
48. Gianni-Barrera R, Trani M, Fontanellaz C, et al. VEGF over-expression in skeletal muscle induces angiogenesis by intussusception rather than sprouting. *Angiogenesis.* 2013;16(1):123–136.
49. Kim ES, Serur A, Huang J, et al. Potent VEGF blockade causes regression of coopted vessels in a model of neuroblastoma. *Proc Natl Acad Sci U S A.* 2002;99(17):11399–11404.
50. Li B, Sharpe EE, Maupin AB, et al. VEGF and PlGF promote adult vasculogenesis by enhancing EPC recruitment and vessel formation at the site of tumor neovascularization. *FASEB J.* 2006;20(9):1495–1497.
51. Ricci-Vitiani L, Pallini R, Biffoni M, et al. Tumour vascularization via endothelial differentiation of glioblastoma stem-like cells. *Nature.* 2010;468(7325):824–828.
52. Naxerova K, Brachtel E, Salk JJ, et al. Hypermutable DNA chronicles the evolution of human colon cancer. *Proc Natl Acad Sci U S A.* 2014;111(18):E1889–E1898.
53. Naxerova K, Jain RK. Using tumour phylogenetics to identify the roots of metastasis in humans. *Nat Rev Clin Oncol.* 2015;12(5):258–272.